Journal of Physics D:
Applied Physics

Hysteresis loops of exchange-coupled magnetic nanoparticle clusters

To cite this article: Mathias Kure *et al* 2025 *J. Phys. D: Appl. Phys.* **58** 185001

OPEN ACCESS
IOP Publishing
Journal of Physics D: Applied Physics
J. Phys. D: Appl. Phys. **58** (2025) 185001 (10pp)
https://doi.org/10.1088/1361-6463/adbf2e

Hysteresis loops of exchange-coupled magnetic nanoparticle clusters

Mathias Kure[1], Frederik L Durhuus[1], Cathrine Frandsen[1,*] and Marco Beleggia[2,3]

[1] DTU Physics, Technical University of Denmark, DK-2800 Kgs. Lyngby, Denmark
[2] DTU Nanolab, Technical University of Denmark, DK-2800 Kgs. Lyngby, Denmark
[3] Department of Physics Informatics and Mathematics, University of Modena and Reggio Emilia, IT-40125 Modena, Italy

E-mail: cfra@dtu.dk and marco.beleggia@unimore.it

Received 24 December 2024, revised 5 March 2025
Accepted for publication 11 March 2025
Published 3 April 2025

Abstract

Experimental evidence indicates that significant exchange coupling may exist between magnetic nanoparticles (MNPs) in dense MNP aggregates such as nanoflower clusters. Here, we examine the role of inter-particle exchange interactions in determining the magnetic properties of MNP clusters, in particular their athermal hysteresis in a low-frequency alternating field. We consider mechanically fixed close-packed clusters where each particle is modeled as a single macrospin coupled to the others by both dipolar interactions and nearest-neighbor exchange. Upon simulating the quasi-static hysteresis curves, we compute the loop area, remanent moment and coercive field, and we classify each curve by its shape. Computing curve types across parameter space reveals how their shape is determined by the interplay between exchange coupling, dipolar interactions, and uniaxial anisotropy. Strong exchange coupling produces fully saturated loops with coherent moment rotation. Moderate exchange and anisotropy result in magnetically soft clusters with high susceptibility. Finally, for complex clusters, weak to moderate exchange and strong anisotropy may produce highly irregular curves with several abrupt changes in magnetization. Our analysis demonstrates that exchange coupling between MNPs significantly increases the cluster energy product, thereby contributing to explain the exceptional heating power of nanoflowers.

Keywords: magnetic nanopaticles, hysteresis heating, dipolar interactions, exchange interactions, magnetic susceptibility

1. Introduction

Magnetic nanoparticles (MNPs) have generated great interest for a wide range of applications [1–5]. Among them is their magnetic heating for therapeutic [6, 7] and catalytic [8, 9] purposes. Several experimental studies [7, 10–15] revealed an enhanced magnetization and heat production capacity of certain nanoparticle clusters referred to as 'nanoflowers'. However, the origin of this phenomenon is yet to be properly understood.

It is well-established that below a material-dependent critical size, atomic exchange interactions ensure that individual MNPs are essentially uniformly magnetized [16], i.e. single-domain. In nanoflowers, several MNP cores are connected into a single rigid body, with more or less direct surface contact and varying crystalline ordering depending on synthesis details [17]. It has been proposed [11, 18] and experimentally corroborated [17, 19, 20], that exchange interactions between

* Author to whom any correspondence should be addressed.

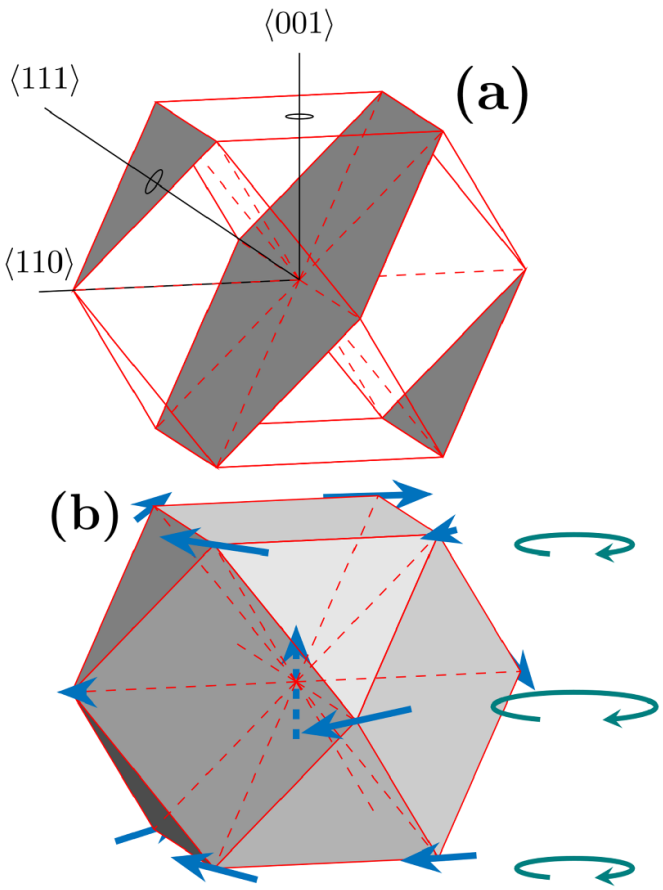

Figure 1. A sketch of the CUB_{13} cluster, i.e. 12 spheres arranged around a central sphere in a *cubic close packed* lattice [28]. (a) The Archimedean solid known as a cuboctahedron, with gray for the hexagonal base plane as well as the top and bottom triangles. The principal directions are shown. (b) The dipolar ground state with magnetic moments placed at the center and vertices. The vertex moments form 3 flux-closed vortices whose directions of rotation are indicated by the circular, teal arrows.

spins at contact surfaces induce a ferromagnetic exchange coupling between adjacent cores, which may explain the unusual magnetic properties of nanoflowers.

In this study, we extend previous work on the theory of magnetostatically coupled MNP clusters [21–27] to include exchange coupling between the single-domain magnetic moments of adjacent particles, which serves as a model of nanoflowers. Note that while nanoflowers are also referred to as multi-core particles, we reserve the terms 'particle' and 'MNP' for the single-domain constituents.

Like in [21, 22], we focus on clusters of identical particles placed in simple geometric configurations, such as MNPs centered on the vertices of a polyhedron, since the high degree of symmetry facilitates the interpretation of the simulated data. Specifically, we consider the simplest possible cluster, the dimer, and the more complex *cuboctahedron*, as shown in figure 1; both the hollow 12-particle cuboctahedron and the 13-particle version of it with the addition of a central magnetic moment, with all calculations restricted to zero temperature. For parameter values, we consider magnetite (Fe_3O_4) and maghemite (γ-Fe_2O_3) MNPs, as these are the most prevalent in biomedical applications due to their relatively low toxicity and high magnetization.

We present a complete analytical solution of dimer ground states and athermal hysteresis, i.e. the response to a slowly varying field, both as a function of the uniaxial anisotropy and effective exchange constant at zero Kelvin. For the cuboctahedron, we do the same by numerical simulations for realistic parameter ranges. The simulated hysteresis curves are labeled by their type (curvature and loop number) and placed into phase diagrams.

2. Model

We consider a collection of identical spherical magnetic nanoparticles (MNPs) bound together in a close-packed cluster and subject to a slowly oscillating, uniform applied field $\mathbf{B}$. We assume both the overall cluster and the individual particles are mechanically fixed, so only the magnetization can change with time. Furthermore, we assume the exchange interaction between the constituent atoms is strong enough that each MNP is uniformly magnetized [16], hence described by a macrospin $\boldsymbol{\mu} = M_0 V \mathbf{m}$ where M_0 is magnetization, V is single-particle volume and $\mathbf{m}$ is a unit vector parallel to the magnetization.

The magnetostatic interaction between uniformly magnetized spheres is that of ideal dipoles [29], which gives the energy contribution

$$E_{\mathrm{dip}} = \frac{\mu_0 \mu^2}{4\pi} \sum_{i<j} \frac{1}{r_{ij}^3} \left[\mathbf{m}_i \cdot \mathbf{m}_j - 3 \left(\mathbf{m}_i \cdot \hat{\mathbf{r}}_{ij} \right) \left(\mathbf{m}_j \cdot \hat{\mathbf{r}}_{ij} \right) \right] \tag{1}$$

with $\mathbf{r}_{ij} = \mathbf{r}_j - \mathbf{r}_i$ the center-to-center displacement vector from MNP i to MNP j, $r_{ij} = |\mathbf{r}_{ij}|$ the distance and $\hat{\mathbf{r}}_{ij} = \mathbf{r}_{ij}/r_{ij}$ the normalized displacement.

When two MNPs are in contact, there will be an exchange interaction between the atomic spins at the contact surface favoring magnetization alignment of the whole MNP pair. This produces a kind of macro exchange coupling between the single-domain moments, which we describe by a nearest-neighbor (NN) Heisenberg model. Thus the exchange energy takes the form

$$E_{\mathrm{exc}} = -\frac{J_{\mathrm{exc}}}{2} \sum_i \sum_{j \in \mathrm{NN}_i} \mathbf{m}_i \cdot \mathbf{m}_j, \tag{2}$$

where J_{exc} is an effective exchange constant with dimensions of energy, NN_i is the set of NNs to particle i and there is a factor $1/2$ to avoid double counting.

We also include Zeeman energy from the applied field and uniaxial anisotropy [30, 31], so the system energy is

$$E = E_{\mathrm{exc}} + E_{\mathrm{Zee}} + E_{\mathrm{ani}} + E_{\mathrm{dip}}, \tag{3}$$

where

$$E_{\mathrm{Zee}} = -\sum_i \boldsymbol{\mu}_i \cdot \mathbf{B}_{\mathrm{app}}, \tag{4}$$

and, introducing the anisotropy constant K and the unit vector $\mathbf{u}$ for the direction of the anisotropy axis,

$$E_{\text{ani}} = -KV\sum_i \left(\mathbf{m}_i \cdot \mathbf{u}_i\right)^2. \tag{5}$$

We note that a characteristic dipole coupling energy is

$$E_0 = \frac{\mu_0 \mu^2}{4\pi D^3}, \tag{6}$$

where D is both particle diameter and smallest interparticle center-to-center distance. We define the dimensionless anisotropy and exchange constants

$$K_{\text{ani}} = \frac{2KV}{E_0} \quad \text{and} \quad J_{\text{eff}} = \frac{J_{\text{exc}}}{E_0}, \tag{7}$$

and use E_0 as an energy unit for the remainder of this article.

We note that with particles of variable size, the distance and degree of surface contact between neighboring MNPs, as well as the number of touching MNPs, will vary within a cluster, such that J_{exc} effectively is different for each MNP. However, an in-depth discussion of non-uniform exchange in clusters is outside the scope of this paper.

3. Dimer analysis

To develop the phenomenology of exchange coupled MNP clusters, we first consider a dimer, i.e. two touching particles. In this case, the dimensionless energy functional is (cf equations (1)–(7))

$$\begin{aligned}\overline{E} = \frac{E}{E_0} &= (1 - J_{\text{eff}})\,\mathbf{m}_1 \cdot \mathbf{m}_2 \\ &\quad - 3\left(\mathbf{m}_1 \cdot \hat{\mathbf{r}}_{12}\right)\left(\mathbf{m}_2 \cdot \hat{\mathbf{r}}_{12}\right) \\ &\quad - \frac{1}{2}K_{\text{ani}}\left[\left(\mathbf{m}_1 \cdot \mathbf{u}_1\right)^2 + \left(\mathbf{m}_2 \cdot \mathbf{u}_2\right)^2\right] \\ &\quad - \overline{\mathbf{B}}_{\text{app}} \cdot \left(\mathbf{m}_1 + \mathbf{m}_2\right)\end{aligned} \tag{8}$$

where we defined the dimensionless applied field

$$\overline{\mathbf{B}}_{\text{app}} = \frac{1}{B_0}\mathbf{B}_{\text{app}}, \quad B_0 = \frac{E_0}{\mu}. \tag{9}$$

We observe that the formal effect of exchange is to modify the first term of the dipole-dipole energy. Normally this term favors antiferromagnetic configurations but for $J_{\text{eff}} > 1$ it turns ferromagnetic.

To illustrate the competing effects, we consider a system with both anisotropy axes along the z-axis ($\mathbf{u}_1 = \mathbf{u}_2 = \hat{\mathbf{z}}$), the displacement vector along the x-axis ($\hat{\mathbf{r}}_{12} = \hat{\mathbf{x}}$) and an applied field oscillating slowly along the x-axis ($\hat{\mathbf{B}}_{\text{app}} = \hat{\mathbf{x}}$).

3.1. Zero-field ground state

We know *a priori* that both magnetic moments of the dimer will remain in the xz-plane since every term in (8) is either isotropic, or favours alignment along the x- or z-axis. Thus, we can represent the full configurational space with the two angles $\theta_{1,2}$ of $\mathbf{m}_{1,2}$ with respect to vertical. The energy landscape in zero-field is then

$$\begin{aligned}\overline{E}\left(B_{\text{app}} = 0\right) = &-\frac{1}{2}K_{\text{ani}}\left(\cos^2\theta_1 + \cos^2\theta_2\right) \\ &+ \left(1 - J_{\text{eff}}\right)\cos\left(\theta_1 - \theta_2\right) - 3\sin\theta_1 \sin\theta_2.\end{aligned} \tag{10}$$

Since (10) is symmetric under $\theta_{1,2} \to -\theta_{1,2}$ we can restrict both angles to the interval $[0, \pi]$ without loss of generality.

Minimizing (10), we find two types of ground states without exchange as illustrated in figure 2(a): one with antiparallel moments along the anisotropy axes, and one with parallel moments along the interparticle axis; the second being the dipolar ground state. Figure 2(a) also illustrates how exchange, if sufficiently strong, can work together with anisotropy to create a third option: ferromagnetic alignment along the anisotropy axes.

Interestingly, there is a triple point at $K_{\text{ani}} = 3, J_{\text{eff}} = 1$ where all configurations with either $\theta_2 = \theta_1$ or $\theta_2 = \pi - \theta_1$ have equal energy, including the three ground state types, in which case the dimer behaves like a perfectly isotropic magnet.

3.2. Dimer hysteresis

For zero-temperature, quasi-static hysteresis, the system will always move to the lowest energy configuration that is accessible without crossing any energy barriers. Thus, one must consider not only extremal points, but the full path through configuration space at a given applied field.

In the present case, where $\mathbf{B}_{\text{app}} \parallel \mathbf{r}_{12}$ and $\mathbf{B}_{\text{app}} \perp \mathbf{u}_{1,2}$, symmetry dictates that on the minimum energy path, $\mathbf{m}_1$ and $\mathbf{m}_2$ will have the same angle with respect to $\mathbf{B}_{\text{app}}$. This limits the analysis to two pathways: co-rotating ($\theta_1 = \theta_2 = \frac{\pi}{2} - \theta$) and counter-rotating ($\theta_1 = \frac{\pi}{2} + \theta, \theta_2 = \frac{\pi}{2} - \theta$). Since the energy is the same whether $\mathbf{m}_1$ rotates clockwise or counterclockwise, we can restrict θ to the interval $[0, \pi]$. Inserting in (10) and adding the Zeeman term, we get

$$\begin{aligned}\overline{E} = &\left(1 - J_{\text{eff}}\right)\cos\left(\theta - p\theta\right) - 3\cos^2\theta \\ &- K_{\text{ani}}\sin^2\theta - 2\overline{B}_{\text{app}}\cos\theta,\end{aligned} \tag{11}$$

where $p = +1$ for co-rotation and $p = -1$ for counter-rotation. We see that counter-rotation is lower in energy, hence will occur, whenever $J_{\text{eff}} < 1$, while co-rotation occurs for $J_{\text{eff}} > 1$. When $J_{\text{eff}} = 1$, the two are energetically equal.

Solving $\frac{\mathrm{d}}{\mathrm{d}\theta}\overline{E} = 0$ shows that the extremal points are precisely $\theta = 0, \pi$ and a critical angle obeying

$$\cos\theta_{\text{crit}} = \frac{\overline{B}_{\text{app}}}{K_{\text{ani}} - 3 - \left(1 - J_{\text{eff}}\right)\left(1 - p\right)} \tag{12}$$

when (12) has a real-valued solution.

Now consider a strong enough negative field that $\theta = \pi$ and let it increase slowly. The dimer will then transition from $\theta = \pi$ to θ_{crit} as soon as $\overline{E}(\theta_{\text{crit}}) = \overline{E}(\pi)$, as there can be no energy barriers in between. This amounts to a second order equation in

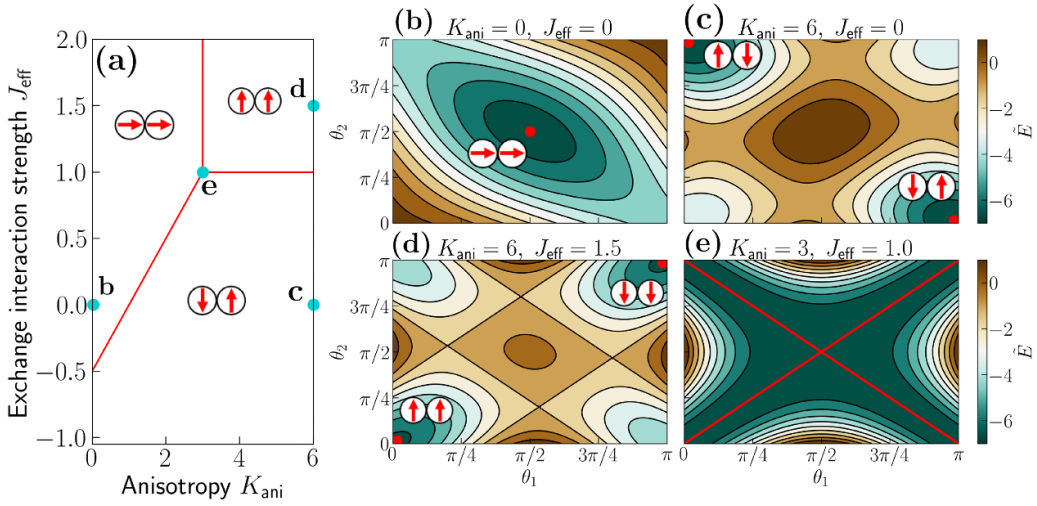

Figure 2. (a) Phase diagram for the zero-field ground state of the dimer, featuring 3 distinct regions depending on the magnitudes of the anisotropy and exchange energy relative to dipolar: dipolar ground state and parallel- or antiparallel along the anisotropy axis. (b)–(e) Energy landscapes for selected parameter pairs corresponding to the turquoise points in the phase diagram. Energy is color-coded and degenerate ground states are indicated in red with sketches of the moment configurations adjacent. The triple point (e) of the phase diagram reveals a quasi-isotropic state where moments are free to rotate coherently at any angle, provided they stay either parallel or antiparallel.

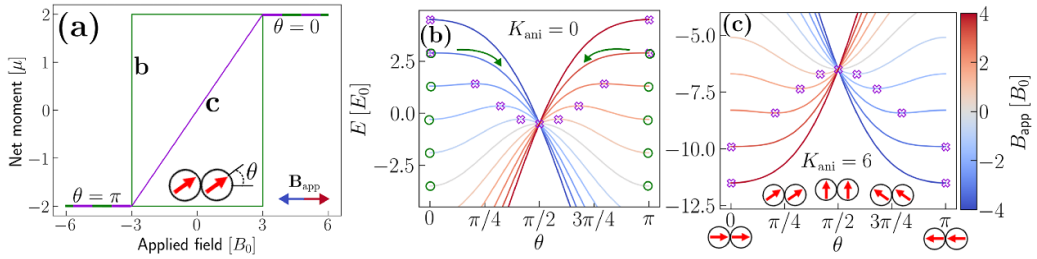

Figure 3. (a) Quasi-static hysteresis loops for the exchange-coupled dimer, where $K_{ani} = 0$ (green curve) and $K_{ani} = 6$ (purple curve). $J_{eff} = 1.5$ for both loops, so the co-rotating pathway is taken. The two loops correspond to the energy paths shown in (b) and (c), respectively. The corresponding θ definition is shown in (a) and example configurations in (c) above and below the corresponding tickmarks. (b)–(c) Energy vs. θ and field amplitude, cf color bar for B_{app}. The critical angles θ_{crit}, for each B_{app} value are indicated by purple crosses. In (b) the crosses are energy maxima, and the equilibrium configurations which produce the green curve in (a) are indicated by green circles. The green arrows mark the two sudden moment reversals. In (c) the θ_{crit} values are local minima, hence they are also the equilibrium angles which produce the purple curve in (a).

B_{app} for both pathways, with the lower value being the critical transition field:

$$\overline{B}_{crit} = \begin{cases} 3 - K_{ani}, & J_{eff} \geqslant 1 \\ 1 - K_{ani} + 2J_{eff}, & J_{eff} \leqslant 1. \end{cases} \tag{13}$$

When $\overline{B}_{crit} < 0$, then $\overline{E}(0) > \overline{E}(\pi)$ so θ_{crit} must be a global minimum, hence when increasing B_{app} further, the configuration follows θ_{crit} and the magnetization $M \sim \cos\theta$ varies linearly in B_{app} until saturation. This is exemplified in figure 3(c), which shows a global minimum at θ_{crit} for all B_{app} values as indicated by the purple crosses. Figure 3(a) shows the corresponding magnetization vs. B_{app} (purple curve) which is indeed linear until saturation. The loop area is zero, and we can calculate a finite dimer susceptibility from

$$\chi = \frac{\mathrm{d}M}{\mathrm{d}H_{app}} = \frac{\mu_0 \mu}{B_0 V} \frac{\mathrm{d}\cos\theta}{\mathrm{d}\overline{B}_{app}} = 24 \frac{\mathrm{d}\cos\theta}{\mathrm{d}\overline{B}_{app}},$$

and (12), i.e.

$$\chi\Big|_{\overline{B}_{crit} < 0} = \frac{24}{K_{ani} - 3 - (1 - J_{eff})(1 - p)}. \tag{14}$$

To get the susceptibility of a sample of dimers, with no inter-dimer interactions, multiply χ by the volume fraction of dimers [32].

If instead $\overline{B}_{crit} \geqslant 0$, then $\overline{E}(0)$ is the global minimum, so the moments suddenly flip from $\theta = \pi$ to 0 when $B_{app} = \overline{B}_{crit}$, and likewise from $\theta = 0$ to π when lowering the field back to $B_{app} = -\overline{B}_{crit}$. This amounts to a rectangular hysteresis curve with $\overline{B}_{crit}$ as the coercive field. An example is shown in figure 3(b) where, following the green circles from the red curve ($B_{app} = 4\,B_0$) to the blue curve ($B_{app} = -4\,B_0$) and back again, the equilibrium angle (green circle) is 0 or π throughout with two sudden flips (green arrows) which produces the rectangular (green) hysteresis curve in figure 3(a). The area of

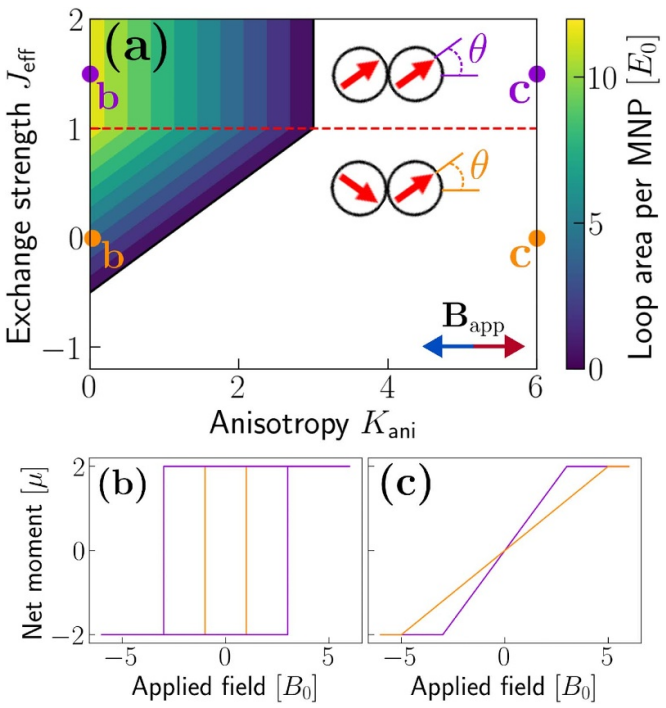

Figure 4. (a) Area of the dimer hysteresis loop per particle as function of the anisotropy and exchange parameters. White means zero hysteresis. Above (below) the red dashed line where $J_{\text{eff}} = 1$, the moments reverse by the co-rotating (counter-rotating) pathway as illustrated. (b)–(c) Example hysteresis curves with parameters indicated in (a) (all combinations of $K_{\text{ani}} = 0, 6$ and $J_{\text{eff}} = 0, 1.5$).

the dimer hysteresis loop is then simply

$$A_{\text{loop}} = 2\,(2\mu) \times 2B_{\text{crit}} = 8\overline{B}_{\text{crit}} E_0. \tag{15}$$

From (12)–(15) we see that exchange increases the susceptibility and hysteresis area up to $\chi = 24/(K_{\text{ani}} - 3)$ and $A_{\text{loop}}/E_0 = 8(3 - K_{\text{ani}})$ for $J_{\text{eff}} \geqslant 1$. Increasing J_{eff} above 1 has no effect because the exchange energy is constant for the co-rotating pathway. Our results on dimer hysteresis are summarized in figure 4. Comparing to figure 2, it is evident that the hysteresis curve opens precisely when the dipolar energy minimum is the ground state. Also, the largest loop area occurs for strong dipolar coupling E_0 and exchange J_{eff}, but decreases with anisotropy. This is because for both pathways dipolar interactions increase the energy difference between moments aligned with the field and the intermediate, perpendicular state ($\theta = \frac{\pi}{2}$), while the anisotropy decreases the energy of the $\theta = \frac{\pi}{2}$ state, thus lowering the energy barrier.

4. Cuboctahedron analysis

4.1. Model cluster

As a model system we consider the cuboctahedron cluster, i.e. we place one MNP at each of the twelve vertices in a cuboctahedron (see figure 1). We consider this structure both with a central particle, (Cub_{13}) and without (Cub_{12}). The Cub_{13} can also be viewed as a subset of a *cubic close packed* lattice [28]. The advantages of the cuboctahedron are that it is well defined and unlike the dimer it has complex multi-particle interactions in 3-dimensions, yet the 12 vertex particles are symmetric with the same number of NN which greatly simplifies the data interpretation. Also, close-packing is to be expected in real MNP clusters due to van der Waals attraction [33].

Whether or not the Cub_{13} occurs naturally is unclear; nevertheless, the Cub_{13} should resemble real clusters enough to generalize trends and qualitative observations. A comparison with the hollow Cub_{12} serves to illuminate the effect of adding the central particle. While most nanoflowers have a magnetic core, they can be synthetized with a non-magnetic center (see NF4 in [17]), and hollow MNPs are both possible and have a number of advantages [34], e.g. in drug transport [35].

Including uniaxial anisotropy adds the choice of anisotropy axis direction for each particle, $\mathbf{u}_i$, which in reality is likely to depend on the cluster formation process. One option is to have $\mathbf{u}_i$ oriented along the ground state configuration of the magnetic moments. This is the global energy minimum, and hence it may be likely to occur for clusters formed by slow self-assembly in zero-field. Another option is a random distribution of anisotropy axes, which may represent scenarios where the assembly process is quenched rapidly from high temperature. Alternatively, one may consider all anisotropy axes aligned with one of the high-symmetry directions labeled in figure 1, which seems reasonable for clusters grown via oriented attachment [36–38] and thermal annealing. To limit the scope of this study we only simulate the latter case with all anisotropy axes along $\langle 001 \rangle$.

Analogously to the dimer, we determine area, remanence and coercive field as functions of K_{ani} and J_{eff}, but for the Cub_{12} and Cub_{13} we obtain all results by numerical simulations.

4.2. Computational framework

The goal is to simulate the quasi-static hysteresis curve $\boldsymbol{\mu}_{\text{tot}}(\mathbf{B}_{\text{app}})$ where $\boldsymbol{\mu}_{\text{tot}} = \sum_i \boldsymbol{\mu}_i$ is the net cluster moment. By quasi-static, we mean that $\boldsymbol{\mu}_{\text{tot}}$ is allowed to relax after each update of the applied field, so the system moves adiabatically between equilibrium moment configurations. This corresponds to the hysteresis in a slowly oscillating magnetic field at zero temperature.

The stationary solutions are precisely those where $\boldsymbol{\mu}_i$ is parallel to the effective field on particle i, which is defined by

$$\mathbf{B}_i^{\text{eff}} = -\frac{1}{\mu}\frac{\delta E}{\delta \mathbf{m}_i} = \mathbf{B}_{\text{app}} + \mathbf{B}_i^{\text{dip}} + \mathbf{B}_i^{\text{ani}} + \mathbf{B}_i^{\text{exc}} \tag{16}$$

where

$$\mathbf{B}_i^{\text{dip}} = \frac{\mu_0 \mu}{4\pi} \sum_{j \neq i} \frac{1}{r_{ij}^3} \left[3\,(\mathbf{m}_i \cdot \hat{\mathbf{r}}_{ij})\,\hat{\mathbf{r}}_{ij} - \mathbf{m}_j\right] \tag{17}$$

is the dipole field on particle i from every other MNP,

$$\mathbf{B}_i^{\text{ani}} = \frac{2K}{M_0}\,(\mathbf{m}_i \cdot \mathbf{u}_i)\,\mathbf{u}_i, \tag{18}$$

is the anisotropy field of particle i and

$$\mathbf{B}_i^{\text{exc}} = \frac{J_{\text{eff}}}{\mu} \sum_{j \in \text{NN}_i} \mathbf{m}_j. \tag{19}$$

is the effective exchange field from all NNs on particle i

At each applied field step, we employ the Molecular Dynamics method in [21] to relax $\mathbf{m}_i$ into the equilibrium state, computing the full instantaneous value of $\mathbf{B}_i^{\text{eff}}$ iteratively until convergence. The moment configuration of the previous step is used as initial state. The first step of each curve is initialized with random starting orientations of the moments at the maximum applied field.

Given an expression for $\mathbf{B}_{\text{eff}}$, one could simulate the full time evolution of the system using the LLG equation [39], as is done in micromagnetics [40–42]. However, while the time scales and transient dynamics of the present method are unphysical, it yields the same stationary solutions and adiabatic dynamics as the LLG, at a lower computational cost.

4.3. Realistic parameter values

As example MNPs we consider maghemite spheres with diameter $D = 10$ nm, so the magnetization is $M_0 = 380\,\text{kA}\,\text{m}^{-1}$ and the particle moment is $\mu = 0.20\,\text{A}\,\text{nm}^2$, which means the dipolar reference energy is (cf (6)) $E_0 = 3.96 \times 10^{-21}$ J, or in thermal units $E_0/k_{\text{B}} = 287$ K where k_{B} is Boltzmann's constant.

We are not aware of any studies on the strength of exchange coupling between maghemite particles. However, Mössbauer measurements of antiferromagnetic iron oxide hematite (α-Fe_2O_3) nanoparticles indicate exchange coupling on the order of 600 K, [43–45], corresponding to $J_{\text{eff}} \sim 2$ if the same coupling is established between 10 nm maghemite particles. The hematite particles were of size $D = 20$ nm and $D = 8$ nm. These studies used antiferromagnetic nanoparticles with negligible dipolar interactions to isolate the effect of macrospin exchange.

Contrary to exchange interactions, anisotropy constants are well documented for maghemite nanoparticles. For 10 nm diameter spheres, the value is close to the bulk magnetocrystalline anisotropy of $20\,\text{kJ}\,\text{m}^{-3}$, although the anisotropy increases greatly for smaller particles due to surface effects [46]. The corresponding anisotropy energy is (cf (5)) $E_{\text{ani}} = 1.0 \times 10^{-20}$ J or equivalently $E_{\text{ani}}/k_{\text{B}} = 760$ K, which translates to $K_{\text{ani}} = 2.65$.

In conclusion, dipolar energy is typically lower than anisotropy and exchange, but all fall within an order of magnitude for 10 nm diameter maghemite particles.

4.4. Ground state

Simulating the CUB_{12} at $J_{\text{eff}}, K_{\text{ani}} = 0$ we find that in the dipolar ground state, the moments form three co-rotating, flux-closed vortices in the plane perpendicular to $\langle 001 \rangle$, yielding a high toroidal moment [47] and zero net magnetization. For the CUB_{13} the central moment points along $\langle 001 \rangle$ which induces a slight out-of-plane tilt in the outer moments as indicated in figure 1(b). The net moment is $\mu_{\text{net}} = 1.0021$, essentially just that of the central particle. The orientations of the MNP moments are determined by the dipolar interactions, which create an effective cluster anisotropy. This configurational dipolar anisotropy is present even when the particle anisotropy $K_{\text{ani}} = 0$.

It is to be expected that for an increasing value of J_{eff}, the ground state will be uniform in the sense that all macrospins are aligned. Indeed, [48] have given the critical crossover from the flux-closed state to the uniform state to be $J_{\text{eff}} \approx 1$ for an infinite array of randomly placed dipoles. Using the disappearance of the toroidal moment [47] as a marker, we find that the transition occurs at $J_{\text{eff}} \approx 2$ for CUB_{12} and $J_{\text{eff}} \approx 1.3$ for CUB_{13}. The reason for the lower number in CUB_{13} is that exchange interactions are strengthened by the many NN that the central moment has. For both CUB_{12} and CUB_{13}, the uniform ground state is in the $\langle 001 \rangle$ directions.

4.5. Hysteresis without anisotropy

For hysteresis simulations there is the question of the applied field direction. If the cluster as a whole can rotate mechanically, it can find a preferred orientation relative to the field dynamically. On the other hand, if stuck to a surface or otherwise immobilized, there is a fixed orientation of the cluster relative to the applied field direction. Since all magnetic response to linear order, such as the susceptibility tensor, can be reconstructed from the response along three linearly independent axes, we limit our analysis to applying a field along the principal directions $\langle 001 \rangle, \langle 110 \rangle$ and $\langle 111 \rangle$.

We simulated hysteresis curves as described in section 4.2. The loop areas are shown in figure 5 as a function of J_{eff} for both the CUB_{12} and the CUB_{13} with the applied field along each of the principal directions in figure 1(a).

Figure 5(a) shows that exchange interactions generally increase the loop area. The areas are largest when a central moment is present, and there is a significant increase in loop area for CUB_{13} when the field is in the $\langle 001 \rangle$ direction, i.e. the easy direction of net magnetization determined by the cluster anisotropy described above. However, there seems to be an optimal value around $J_{\text{eff}} \approx 1.25$ no matter the field direction, after which the loop area declines steadily.

In figure 5(b), we show a range of curves for the CUB_{13} in the $\langle 001 \rangle$ direction. For the dipolar-only curve ($J_{\text{eff}} = 0$), the net moment, stemming almost exclusively from the central moment, is low. However, the moments are hard to align due to dipolar interactions favoring flux-closure, which leads to a larger coercive field and loop area compared to the first few curves with $J_{\text{eff}} > 0$. In fact, for $J_{\text{eff}} = 0.33$ the hysteresis loop closes entirely. At ($J_{\text{eff}} = 0.67$), after the dip in area described above, the remanent moment is greatly increased at the cost of a slightly smaller coercive field. Increasing J_{eff} more leads to a further enhancement of the remanent moment towards a fully aligned state at zero field. After zero-field saturation is achieved around $J_{\text{eff}} \sim 1.5$, stronger exchange gradually reduces the hysteresis area. This makes sense because the cluster anisotropy becomes relatively less important with

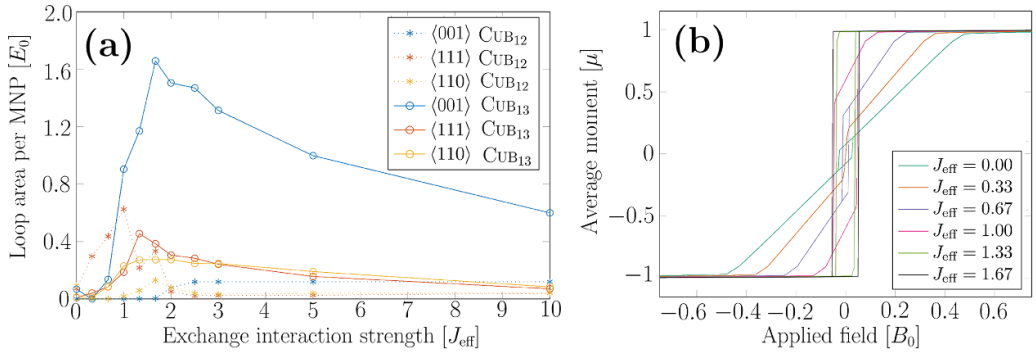

Figure 5. (a) Comparison of hysteresis loop areas with increasing exchange interaction at zero anisotropy. Each data series corresponds to the hysteresis loop area for a field direction along the principal directions of the CUB12 (stars, dashed lines) and the CUB13 (circles, full lines) in the range $J_{\text{eff}} = 0$ to $J_{\text{eff}} = 10$. (b) Hysteresis curves of CUB13 in the ⟨001⟩ direction for increasing values of J_{eff}.

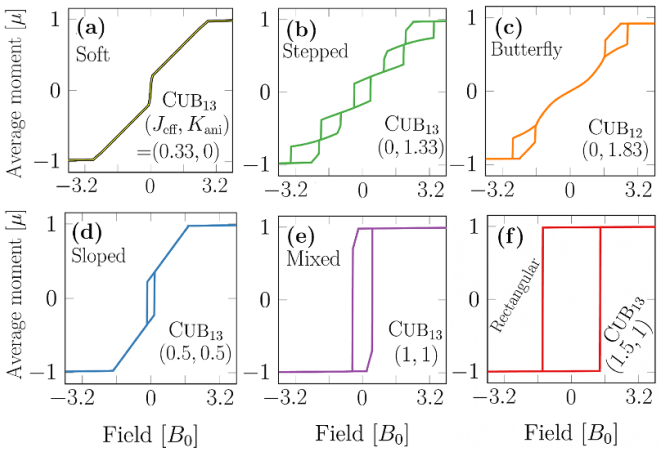

Figure 6. Examples of all the hysteresis curve types we observed. The corresponding parameter values are indicated in the bottom right by CUB12 or CUB13 (J_{eff}, K_{ani}).

strong exchange, until the limit of $J_{\text{eff}} \to \infty$ where the cluster behaves like a single, uniformly magnetized particle.

We note that the dimer studied above has the largest hysteresis area for high J_{eff} when the moments rotate coherently. The difference is that a uniformly magnetized dimer has significant shape anisotropy, while the cuboctahedron is nearly isotropic. Another difference is that, since the cuboctahedron simulations have field and anisotropy axes parallel, the uniaxial anisotropy acts as an energy barrier, thereby increasing loop area. Conversely, the dimer has perpendicular anisotropy, which reduces the energy of the intermediate state.

4.6. Hysteresis with anisotropy

The different hysteresis curve types we observe along ⟨001⟩ are shown in figure 6, while a phase diagram of curve type vs. $J_{\text{eff}}, K_{\text{ani}}$ is shown in figure 7 for CUB12 and CUB13, together with the distribution of hysteresis loop areas.

For the CUB12 a soft curve with zero hysteresis is seen when dipolar coupling dominates (low $K_{\text{ani}}, J_{\text{eff}}$), while the combination of high exchange and anisotropy leads to rectangular loops. More exotic is the butterfly curves occurring for low exchange and high anisotropy (figure 6(c)). Double-loop curves with zero-remanence are known from disc-shaped MNPs [49], though those tend to be rectangular while the butterfly curve (figure 6(c)) has a variable, finite slope and more complex loops. In both cases, there are three qualitatively different equilibrium states depending on the applied field (vortex and uniformly magnetized up/down), hence two energy barriers and two loops.

For the CUB13 there is a smaller region of soft loops for low $K_{\text{ani}}, J_{\text{eff}}$ (figure 6(a)). At moderate exchange and anisotropy, the central moment opens up the curve, leading to the sloped- and mixed curves (figures 6(d) and (e)). Instead of the butterfly curve when anisotropy dominates, we find the stepped curve (figure 6(b)), which has two symmetric pairs of loops for positive/negative field and one central loop. The reason for the greater subloop number of CUB13 (figure 6(b)) compared to CUB12 (figure 6(c)) is that the CUB13 attains 6 states due to the central moment: up/down uniform, vortex with up/down central moment and two in between, perhaps with central moment opposite the rest. This amounts to 5 energy barriers, hence 5 subloops. We find that depending on the exact K_{ani} and J_{eff} values, these loops may close or merge, often yielding a single stepped loop or 3 separate ones, but always an odd number and never more than 5.

The soft/sloped, sloped/mixed and mixed/rectangular transitions are all continuous in terms of loop area (see figure 7), with one curve type smoothly merging into another as J_{eff} or K_{ani} is varied. Conversely, the transition to stepped loops is discontinuous in area, especially the stepped/sloped transition for $J_{\text{eff}} \sim 0.5$.

4.7. Coercive field and remanent moment

From the hysteresis loops calculated above for CUB13, we have also extracted the remanent moment (net moment at zero field) and the coercive field, defined as the field magnitude where the hysteresis curve crosses zero moment. The two plots can be seen in figures 8(a) and (b).

Focusing first on the remanent moment as shown in figure 8(a), the magnetization is saturated for the entire rectangular curve region (red) and approximately half of the mixed region (purple). Otherwise the remanence is seen to increase

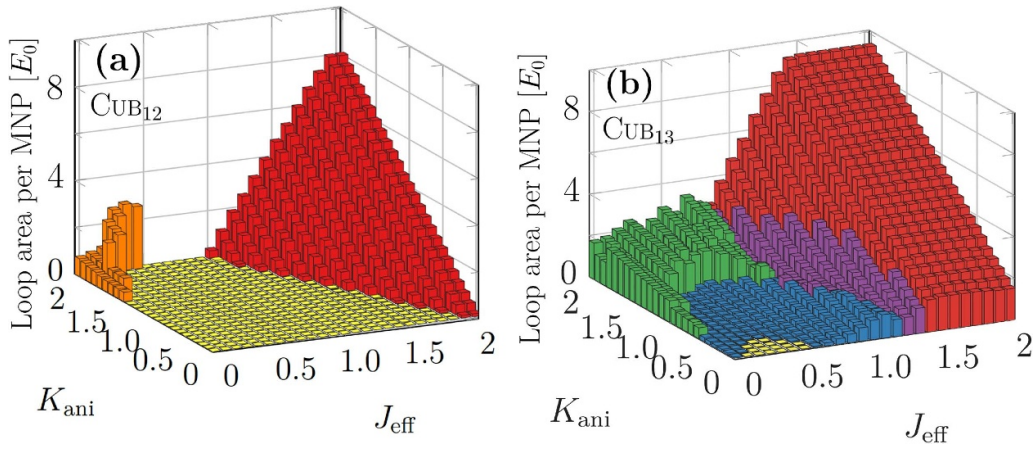

Figure 7. Phase diagrams showing the distribution of loop types with the same colorcoding as figure 6. Each bar is a single simulation with the height indicating the hysteresis loop area per particle.

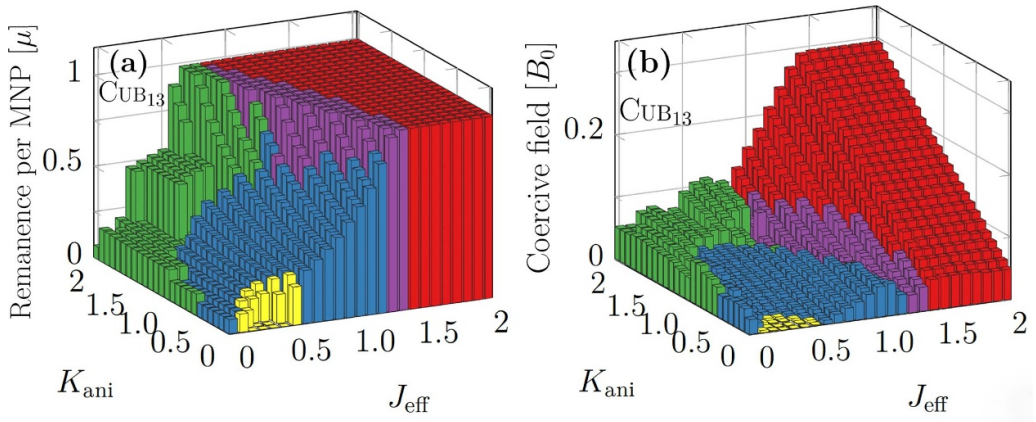

Figure 8. (a) The remanent moment extracted from the hysteresis loops given in figure 7(b). (b) Coercive field of the same loops. Colors indicate loop type with the same colorcoding as figures 6 and 7.

with both exchange and anisotropy, except at two plateaus in the stepped curve region (green) and one plateau for soft curves (yellow).

The reason for the discontinuous remanence for the stepped curves is that, as mentioned in section 4.6, the system cycles through 6 different equilibrium configurations as the applied field oscillates, which come in degenerate pairs. Varying the exchange strength tunes which of the 3 degenerate pairs are ground states, leading to three sub-regions.

It is also visible in figure 8 that not all the soft curves have zero net moment. For example the $J_{\text{eff}} = 0.33$ case in figure 5(b), which is only possible with zero hysteresis if the curve is vertical at $B_{\text{app}} = 0$; this entails infinite susceptibility. We also note that, aside from transitions to and from the three plateaus, remanence appears a continuous function of K_{ani} and J_{eff}.

For $J_{\text{eff}} \geqslant 1$ the coercive field largely follows the loop area, since the loop area is proportional to it for single-loop curves such as the rectangular, sloped and mixed. For multi-loop curves like the stepped, our definition of coercivity only relates to the central loop, not the full area. However, we still observe a strong correlation.

In terms of applications, our analysis reveals that high anisotropy and exchange is especially useful for hysteresis heating. This is because in these conditions the cluster maximizes the absolute energy absorption and because the rectangular loops have the highest ratio of loop area to coercivity. Since the energy cost of generating the applied field scales as B_{app}^2, this implies the greatest energy efficiency. If, instead, high susceptibility with minimal energy dissipation is required, for example in imaging techniques [4, 5] or in power electronic applications to reduce energy losses [50, 51], then the soft curves occurring for moderate but non-zero exchange and anisotropy are ideal. Finally, stepped curves can be tuned between many different moment configurations by modulating the amplitude of a uniform applied field. These may have applications in information processing and storage, or in controllable self-assembly.

5. Conclusions

We have investigated the effect of inter-particle exchange interactions and uniaxial anisotropy on the quasi-static

athermal hysteresis of MNP clusters with the simple dimer and the more complex cuboctahedron as model clusters.

We have shown that anisotropy tends to enhance the cluster energy product (hysteresis loop area) when the anisotropy axis is parallel to the applied field, and to diminish it when perpendicular. The primary role of exchange is generally to increase loop area in both cases, which indicates that interparticle exchange coupling is an important parameter to consider in explaining the exceptional heating power of nanoflowers.

The hollow cuboctahedron cluster, i.e. 12 MNPs fixed at the vertices of said Archimedean solid, was shown to have its hysteresis significantly increased by the addition of a central particle (creating the CUB_{13} cluster). For the CUB_{13} at zero anisotropy, there is an optimum exchange constant of $J_{\mathrm{eff}} \sim 2$ that maximizes loop area. Increasing J_{eff} further gradually reduces the loop area until the $J_{\mathrm{eff}} \to \infty$ limit where the whole cluster behaves like an isotropic, single-domain particle. Overall, our results suggest that optimal tuning of J_{eff} can facilitate the design of better heating agents for biomedicine and catalysis.

By systematically varying K_{ani} and J_{eff} in the range $[0,2]$, we identified 6 qualitatively different hysteresis curve categories. For the CUB_{13}, rectangular loops with moments fully aligned were found for $J_{\mathrm{eff}} \gtrsim 1$, with a shift towards lower J_{eff} as K_{ani} increases. For weak to moderate exchange and anisotropy ($K_{\mathrm{ani}}, J_{\mathrm{eff}} \lesssim 0.5$) we find magnetically soft clusters with high initial susceptibility, which might be useful in diagnostic techniques like magnetorelaxometry [4] and magnetic particle imaging [5], and in electronics [50, 51]. For $K_{\mathrm{ani}} \geqslant 1$ and $J_{\mathrm{eff}} \leqslant 1$ we instead find stepped curves, with up to 5 small hysteresis loops traversed in each field cycle. In this last regime, the equilibrium configuration can be tuned both by uniform applied fields and by the exchange coupling strength, which significantly impacts the net moment and hence the ability to attract other MNPs, with implications for colloidal stability and controlled self-assembly.

When it comes to exchange coupled MNP clusters, there are many promising research directions left to explore, including temperature effects, mechanical motion, hysteresis in a high-frequency applied field, cluster-cluster interactions, clusters of non-identical constituent particles and experimental comparison.

Data availability statement

The data that support the findings of this study are available upon reasonable request from the authors.

Acknowledgments

The authors acknowledge support from the Novo Nordisk Foundation Data Science Research Infrastructure 2022 Grant: A high-performance computing infrastructure for data-driven research on sustainable energy materials, Grant No. NNF22OC0078009.

ORCID iDs

Mathias Kure https://orcid.org/0000-0003-0219-1747
Frederik L Durhuus https://orcid.org/0000-0002-2769-284X
Cathrine Frandsen https://orcid.org/0000-0001-5006-924X
Marco Beleggia https://orcid.org/0000-0002-2888-1888

References

[1] Pankhurst Q A, Connolly J, Jones S K and Dobson J 2003 Applications of magnetic nanoparticles in biomedicine *J. Phys. D: Appl. Phys.* **36** R167
[2] Pankhurst Q A, Thanh N T K, Jones S K and Dobson J 2009 Progress in applications of magnetic nanoparticles in biomedicine *J. Phys. D: Appl. Phys.* **42** 224001
[3] Coene A and Leliaert J 2022 Magnetic nanoparticles in theranostic applications *J. Appl. Phys.* **131** 160902
[4] Liebl M, Wiekhorst F, Eberbeck D, Radon P, Gutkelch D, Baumgarten D, Steinhoff U and Trahms L 2015 Magnetorelaxometry procedures for quantitative imaging and characterization of magnetic nanoparticles in biomedical applications *Biomed. Eng. / Biomed. Tech.* **60**
[5] Yu E Y, Bishop M, Zheng B, Ferguson R M, Khandhar A P, Kemp S J, Krishnan K M, Goodwill P W and Conolly S M 2017 Magnetic particle imaging: a novel invivo imaging platform for cancer detection *Nano Lett.* **17** 1648–54
[6] Rodrigues H F, Capistrano G and Bakuzis A F 2020 *In vivo* magnetic nanoparticle hyperthermia: a review on preclinical studies, low-field nano-heaters, noninvasive thermometry and computer simulations for treatment planning *Int. J. Hyperth.* **37** 76–99
[7] Gavilán H, Kumar Avugadda S, Fernández-Cabada T, Soni N, Cassani M, Mai B T, Chantrell R and Pellegrino T 2021 Magnetic nanoparticles and clusters for magnetic hyperthermia: optimizing their heat performance and developing combinatorial therapies to tackle cancer *Chem. Soc. Rev.* **50** 11614–67
[8] Almind M R, Vinum M G, Wismann S T, Hansen M F, Vendelbo S B, Engbæk J S, Mortensen P M, Chorkendorff I and Frandsen C 2021 Optimized CoNi nanoparticle composition for curie-temperature-controlled induction-heated catalysis *ACS Appl. Nano Mater.* **4** 11537–44
[9] Mortensen P M, Engbæk J S, Vendelbo S B, Hansen M F and Østberg M 2017 Direct Hysteresis heating of catalytically active Ni–Co nanoparticles as steam reforming catalyst *Ind. Eng. Chem. Res.* **56** 14006–13
[10] Hugounenq P *et al* 2012 Iron oxide monocrystalline nanoflowers for highly efficient magnetic hyperthermia *J. Phys. Chem.* C **116** 15702–12
[11] Lartigue L, Hugounenq P, Alloyeau D, Clarke S P, Lévy M, Bacri J-C, Bazzi R, Brougham D F, Wilhelm C and Gazeau F 2012 Cooperative in iron oxide multi-core nanoparticles potentiates their efficiency as heating mediators and MRI contrast agents *ACS Nano* **6** 10935–49
[12] Del Sol-Fernández S, Portilla-Tundidor Y, Gutiérrez L, Odio O F, Reguera E, Barber D F and Morales M P 2019 Flower-like Mn-doped magnetic nanoparticles functionalized with $\alpha_v\beta_3$ -integrin-ligand to efficiently induce intracellular heat after alternating magnetic field exposition, triggering glioma cell death *ACS App. Mater. Interfaces* **11** 26648–63
[13] Espinosa A, Bugnet M, Radtke G, Neveu S, Botton G A, Wilhelm C and Abou-Hassan A 2015 Can magneto-plasmonic nanohybrids efficiently combine

photothermia with magnetic hyperthermia? *Nanoscale* **7** 18872–7
[14] Jefremovas E M *et al* 2021 Nanoflowers versus magnetosomes: comparison between two promising candidates for magnetic hyperthermia therapy *IEEE Access* **9** 99552–61
[15] Gavilán H, Simeonidis K, Myrovali E, Mazarío E, Chubykalo-Fesenko O, Chantrell R, Balcells L, Angelakeris M, Morales M P and Serantes D 2021 How size, shape and assembly of magnetic nanoparticles give rise to different hyperthermia scenarios *Nanoscale* **13** 15631–46
[16] Brown W F 1968 The fundamental theorem of fine-ferromagnetic-particle theory *J. Appl. Phys.* **39** 993–4
[17] Gavilán H *et al* 2017 Colloidal flower-shaped iron oxide nanoparticles: synthesis strategies and coatings *Part. Part. Syst. Charact.* **34** 1700094
[18] Dutz S 2016 Are magnetic multicore nanoparticles promising candidates for biomedical applications? *IEEE Trans. Magn.* **52** 1–3
[19] Bender P *et al* 2018 Relating magnetic properties and high hyperthermia performance of iron oxide nanoflowers *J. Phys. Chem.* C **122** 3068–77
[20] Bender P, Honecker D and Fernández Barquín L 2019 Supraferromagnetic correlations in clusters of magnetic nanoflowers *Appl. Phys. Lett.* **115** 132406
[21] Kure M, Beleggia M and Frandsen C 2017 Magnetic dipolar ordering and hysteresis of geometrically defined nanoparticle clusters *J. Appl. Phys.* **122** 133902
[22] Hovorka O, Barker J, Friedman G and Chantrell R W 2014 Role of geometrical symmetry in thermally activated processes in clusters of interacting dipolar moments *Phys. Rev.* B **89** 104410
[23] Hovorka O 2017 Thermal activation in statistical clusters of magnetic nanoparticles *J. Phys. D: Appl. Phys.* **50** 044004
[24] Ilg P 2017 Equilibrium magnetization and magnetization relaxation of multicore magnetic nanoparticles *Phys. Rev.* B **95** 214427
[25] Ortega-Julia J, Ortega D and Leliaert J 2023 Estimating the heating of complex nanoparticle aggregates for magnetic hyperthermia *Nanoscale* **15** 10342–50
[26] Barrera G, Allia P and Tiberto P 2021 Heating ability modulation by clustering of magnetic particles for precision therapy and diagnosis *J. Phys. D: Appl. Phys.* **54** 315003
[27] Serantes D, Simeonidis K, Angelakeris M, Chubykalo-Fesenko O, Marciello M, Morales M del P, Baldomir D and Martinez-Boubeta C 2014 Multiplying magnetic hyperthermia response by nanoparticle assembling *J. Phys. Chem.* C **118** 5927–34
[28] Weisstein E W Cuboctahedron from math world–a wolfram web resource (available at: http://mathworld.wolfram.com/Cuboctahedron.html)
[29] Edwards B F, Riffe D M, Ji J-Y and Booth W A 2017 Interactions between uniformly magnetized spheres *Am. J. Phys.* **85** 130–4
[30] Bedanta S, Petracic O and Kleemann W 2015 Supermagnetism *Handbook of Magnetic Materials* vol 23 (Elsevier) pp 1–83
[31] Durhuus F L, Beleggia M and Frandsen C 2024 Conservation laws for interacting magnetic nanoparticles at finite temperature *Phys. Rev.* B **109** 054421
[32] Zambach M, Varón M, Almind M R, Knaapila M, Ouyang Z, Beleggia M, and Frandsen C 2025 Demagnetisation effects in single-domain particles (arXiv:2502.03394)
[33] Durhuus F L, Wandall L H, Boisen M H, Kure M, Beleggia M and Frandsen C 2021 Simulated clustering dynamics of colloidal magnetic nanoparticles *Nanoscale* **13** 1970–81
[34] Khurshid H, Nemati Z, Iglesias O, Alonso J, Phan M-H and Srikanth H 2021 Hollow magnetic nanoparticles *New Trends in Nanoparticle Magnetism* vol 308 D Peddis, S Laureti and D Fiorani (Springer) pp 137–58
[35] Xing R, Bhirde A A, Wang S, Sun X, Liu G, Hou Y and Chen X 2013 Hollow iron oxide nanoparticles as multidrug resistant drug delivery and imaging vehicles *Nano Res.* **6** 1–9
[36] Li D, Nielsen M H, Lee J R I, Frandsen C, Banfield J F and De Yoreo J J 2012 Direction-specific interactions control crystal growth by oriented attachment *Science* **336** 1014–8
[37] Frandsen C *et al* 2005 Oriented attachment and exchange coupling of α-Fe_2O_3 nanoparticles *Phys. Rev.* B **72** 214406
[38] Penn R L and Banfield J F 1999 Formation of rutile nuclei at anatase (112) twin interfaces and the phase transformation mechanism in nanocrystalline titania *Am. Mineral.* **84** 871–6
[39] Gilbert T 2004 A phenomenological theory of damping in ferromagnetic materials *IEEE Trans. Magn.* **40** 3443–9
[40] Bjørk R, Poulsen E, Nielsen K and Insinga A 2021 MagTense: a micromagnetic framework using the analytical demagnetization tensor *J. Magn. Magn. Mater.* **535** 168057
[41] Donahue M J and Porter D G 1999 OOMMF user's guide, version 1.0, *Technical Report* number NIST IR 6376 (Institution National Institute of Standards and Technology)
[42] Vansteenkiste A, Leliaert J, Dvornik M, Helsen M, Garcia-Sanchez F and Van Waeyenberge B 2014 The design and verification of MuMax3 *AIP Adv.* **4** 107133
[43] Hansen M F, Koch C B and Mørup S 2000 Magnetic dynamics of weakly and strongly interacting hematite nanoparticles *Phys. Rev.* B **62** 1124–35
[44] Theil Kuhn L, Lefmann K, Bahl C R H, Ancona S N, Lindgård P-A, Frandsen C, Madsen D E and Mørup S 2006 Neutron study of magnetic excitations in $8-\mathrm{nm}\alpha-Fe_2O_3$ nanoparticles *Phys. Rev.* B **74** 184406
[45] Frandsen C and Mørup S 2005 Spin rotation in α-Fe_2O_3 nanoparticles by interparticle interactions *Phys. Rev. Lett.* **94** 027202
[46] Pisane K, Singh S and Seehra M 2017 Unusual enhancement of effective magnetic anisotropy with decreasing particle size in maghemite nanoparticles *Appl. Phys. Lett.* **110** 222409
[47] Ederer C and Spaldin N A 2007 Towards a microscopic theory of toroidal moments in bulk periodic crystals *Phys. Rev.* B **76** 214404
[48] Kechrakos D and Trohidou K 2003 Competition between dipolar and exchange interparticle interactions in magnetic nanoparticle films *J. Magn. Magn. Mater.* **262** 107–10
[49] Goiriena-Goikoetxea M, Muñoz D, Orue I, Fernández-Gubieda M, Bokor J, Muela A and García-Arribas A 2020 Disk-shaped magnetic particles for cancer therapy *Appl. Phys. Rev.* **7** 011306
[50] Zambach M, Varón M, Knaapila M, Ouyang Z, Beleggia M and Frandsen C 2023 Design of superparamagnetic nanoparticle-materials for high-frequency inductor cores (arXiv:2308.13407)
[51] Sanusi B, Zambach M, Varón M, Beleggia M, Frandsen C and Ouyang Z 2024 Low profile superparamagnetic inductor for portable electronics power management submitted